

Dynamic analysis of detumbling a rotating satellite using flexible deceleration rod

Honghua Dai

Northwestern Polytechnical University

Hao Chen (✉ npuchenhao@mail.nwpu.edu.cn)

Northwestern Polytechnical University <https://orcid.org/0000-0002-3846-1924>

Xiaokui Yue

Northwestern Polytechnical University

Research Article

Keywords: Rotating satellite, Detumbling, Flexible rod, Contact detection

Posted Date: November 30th, 2021

DOI: <https://doi.org/10.21203/rs.3.rs-1054846/v1>

License:  This work is licensed under a Creative Commons Attribution 4.0 International License.

[Read Full License](#)

Version of Record: A version of this preprint was published at Nonlinear Dynamics on April 9th, 2022. See the published version at <https://doi.org/10.1007/s11071-022-07414-6>.

Dynamic analysis of detumbling a rotating satellite using flexible deceleration rod

Honghua Dai^{1,2}, Hao Chen^{1,2*} and Xiaokui Yue^{1,2}

¹National Key Laboratory of Aerospace Flight Dynamics, Northwestern Polytechnical University, Xi'an, 710072, Shaanxi, China.

²School of Astronautics, Northwestern Polytechnical University, Xi'an, 710072, Shaanxi, China.

*Corresponding author(s). E-mail(s): npuchenhao@mail.nwpu.edu.cn;
Contributing authors: hhdai@nwpu.edu.cn; xkyue@nwpu.edu.cn;

Abstract

Malfunctioning satellites are generally non-cooperative tumbling objects. Due to their complex tumbling motion, it is essential to stabilize the target within an acceptable rotating range in the pre-capture phase. In contrast to contactless methods, contact methods based on flexible devices are efficient and can generate sufficient operating torque through flexible contact. However, accurate dynamic analysis of the operation is challenging because of two limitations. It is difficult to obtain a high-efficiency description of the large deformation arising from the operating process. Moreover, the contact between a flexible device and a tumbling object is hard to detect efficiently. This paper proposes a method for detumbling a free-floating rotating satellite; it uses a flexible rod to contact the solar array of the target. The absolute nodal coordinate formulation is first applied to a rod-contact detumbling model in simulation to describe the large deformation of the rod precisely with a low computational burden. Next, a two-step method to detect the contact is employed to pinpoint the contact point and speed up the simulation: coarse detection in the contactless phase and fine detection in the contact phase. Finally, the feasibility of the contact detumbling method is verified. In addition, through the further analysis of the contact process, some characteristics of this kind of strategy are studied for the first time.

Keywords: Rotating satellite, Detumbling, Flexible rod, Contact detection

1 Introduction

With the development of space technology, the amount of debris around the Earth has increased significantly. Recent low Earth orbit (LEO) constellations, such as Starlink and Telesat, are implemented with the launch of thousands of satellites. Malfunctioning and end-of-life satellites become debris in LEO [1, 2] and orbital refueling, repair, and active debris removal will become crucial to preserving the near-Earth environment for future

generations [3, 4]. In-orbit capture will play an essential role in these operations, but it is the most challenging step due to its need for close-range maneuvering and contact with the target [5–7]. However, most malfunctioning and end-of-life satellites are non-cooperative targets that cannot provide useful information actively [8, 9]. Moreover, they are usually rotating, or tumbling, because of residual angular momentum, energy

dissipation, and factors such as the gravity gradient and eddy-current damping [10–12]. All these factors make it difficult to capture such debris [6, 13]. Space objects that tumble at a rate below $3^\circ/s$ can be captured easily; a tumbling rate above $30^\circ/s$ is not regarded as a target; an object tumbling between $3^\circ/s$ and $30^\circ/s$ can be detumbled in advance [14]. Thus, if the object is tumbling rapidly, a fly-around and grasping by a robot arm seem infeasible. It would be indispensable to capture a non-cooperative target if its angular velocity could be reduced in the pre-capture phase.

Many detumbling strategies have been developed for non-cooperative targets. According to the operating torque, these are classified as either contactless or contact methods. The contactless ones reduce the target's angular velocity via contactless forces such as plume impingement and electrostatic force. Nakajima et al. [15, 16] proposed a detumbling method using thruster plume impingement. Bennett and Schaub [17] extended the electrostatic detumble theory to three-dimensional tumbling motion. Gomez and Walker [18–20] developed an eddy-current method to produce an electromagnetic braking torque. Kumar and Sedwick [21] modeled the use of laser ablation to de-spin large space objects before docking. These non-contact strategies make it possible to operate at a safe distance. However, the operating force is small, even for large objects.

Contact methods apply a large torque with high detumbling efficiency, although the contact can pose a collision risk. Hovell and Ulrich [22] proposed a tethered detumbling method where four visco-elastic tethers are attached to chaser spacecraft connected to the target to produce external torque. Wang et al. [23] studied a scheme for de-spinning a target with a tethered space manipulator. Furthermore, a detumbling method based on a flexible device is considered more efficient and safer than other approaches. Nishida and Kawamoto [14] designed a brush-type contactor as an end-effector of the robot arm to reduce a cylindrical object's rotation. Braking torque is produced by friction. Wu et al. [24] developed a flexible brush to de-spin a satellite. However, the cube-like brush made it difficult to control the position and direction of the contact force to avoid increasing nutation. Liu et

al. [25, 26] analyzed the dynamics of detumbling a high dynamic non-cooperative satellite using a flexible device that contacts the target's base. The flexible device model was established by a lumped-mass finite-element method, which had limitations in describing large deformation precisely. Wang et al. [27] focused on the optimal contact control for eliminating the rotation and damping nutation. The small force generated via a brief contact between the end of a spring contactor and a solar array had a low efficiency. In summary, contacting the base of a tumbling satellite involves working at a close distance, which brings a high risk of collision between the robot and other parts, such as sails and aerials. Methods contacting the target sail are safe and efficient and thus suitable for in-orbit service. However, these flexible-device strategies have two problems that hinder accurate dynamic analysis. First, traditional finite-element or lumped-mass methods are limited in precisely describing a large deformation and rotation of the flexible device. Second, methods detecting the contact and pinpointing the contact points are limited in the accuracy and efficiency of the simulation.

Unlike the flexible brush, the flexible rod has only five degrees of freedom that need to be controlled, so it is easier to obtain a precise contact point to avoid increasing nutation. Because the brush is a collection of many thin rods, it is challenging to represent their contact to simulate the operational process accurately. In a study of the detumbling strategy, a rod could be used as a simplified brush model to verify theories and algorithms. Inspired by previous studies, this paper presents a contact detumbling method that uses a flexible rod to operate the satellite sail. The dynamics of the system are modeled to analyze the detumbling process. The contributions of our work are threefold:

1. A detumbling method that uses a flexible rod to contact the outer edge of the solar array is proposed. The equipment can manipulate the target at a safe distance and generate a large operating torque for braking.
2. The absolute nodal coordinate formulation (ANCF) is first applied to the dynamic model

of this detumbling system based on the flexible rod. It can precisely describe large deformation and rotation of the rod with a low computation burden.

3. The contact point moves along the flexible rod in a contact process. The proposed two-step contact-detection method precisely describes the process in detail and lightens the computational burden in the contactless stage.

The rest of this paper is organized as follows: Section 2 establishes the dynamic model of the detumbling system. Then in Section 3, the contact detection method and the contact force model are introduced. Section 4 simulates the detumbling process and analyzes the characteristics of the detumbling method. This paper's conclusions are presented in Section 5.

2 Dynamic model of detumbling system

In this section, The ANCF and the Lagrangian method are employed to model the dynamics of a free-floating malfunctioning satellite and a robot with a flexible deceleration device.

2.1 Model description

The space target shown in Fig.1 has a central rigid body with two long rigid solar arrays. The deceleration device, a flexible rod used as the end-effector of a space manipulator on a chaser spacecraft, can adjust the position and attitude for the detumbling task. Because the solar array is much longer than other parts of the satellite and the spin axis is usually perpendicular to the solar array's lengthwise direction, contacting its outer edge can generate a large decelerating torque resulting in a smooth ,effective momentum transfer. The method also avoids dangerous collisions since the robot maintains a safe distance from the target.

Figure.2 shows the process of contact detumbling: preparation, pre-contact, contact, post-contact. The mission can be divided into the measuring and tracking stage, and the detumbling stage. This paper focuses on the detumbling stage to analyze system dynamics. The controller of the

space robot has a simple design that does not consider the adjustment process of the thruster and space manipulator.

The coordinate frames of the detumbling system are shown in Fig.3. Here, $O - XYZ$ is the global coordinate frame that is fixed in time; $O_1 - X_1Y_1Z_1$, parallel to the frame $O - XYZ$, is a body-fixed coordinate frame of the flexible device whose origin O_1 is situated at the joint of the device; $O_2 - X_2Y_2Z_2$ is a body-fixed frame of the rigid target whose origin O_2 is fixed at the center of mass of the target; $O_3 - X_3Y_3Z_3$ is a body-fixed frame of the robot whose origin O_3 is at the center of mass of the chaser.

2.2 Dynamic equation of deceleration device

The precise dynamical model of the deceleration device rests on the precondition of contact analysis. During the operation, the device counters a large flexible deformation with significant rotation and displacement arising from the space robot. To accurately describe the dynamics of the flexible device, the ANCF, a finite element non-incremental formulation, is applied to the dynamical model of the flexible rod. The operating conditions permit the rod to be represented as an Euler-Bernoulli beam. In the ANCF, nodal coordinates of the element are defined in the global coordinate frame, and consequently no coordinate transformation is required[28–30].

Figure 4 shows the definition of element nodal coordinates, and the original length of the beam element is L , and global nodal coordinates are defined on the neutral axis at $x = 0$ and $x = L$, respectively, as

$$\mathbf{a}_i = [\mathbf{r}^T \ \mathbf{r}_x^T]^T = [r_{iX} \ r_{iY} \ r_{iZ} \ \frac{\partial r_{iX}}{\partial x} \ \frac{\partial r_{iY}}{\partial x} \ \frac{\partial r_{iZ}}{\partial x}]^T \quad (1)$$

The vector of element nodal coordinates can be expressed as

$$\mathbf{e} = [\mathbf{a}_1^T \ \mathbf{a}_2^T]^T \quad (2)$$

The global position vector \mathbf{r} of an arbitrary point P on the neutral axis of a element is defined in terms of nodal coordinates and the element shape function, as

$$\mathbf{r} = \mathbf{S}(x)\mathbf{e} = [s_1\mathbf{I} \ s_2\mathbf{I} \ s_3\mathbf{I} \ s_4\mathbf{I}] \mathbf{e} \quad (3)$$

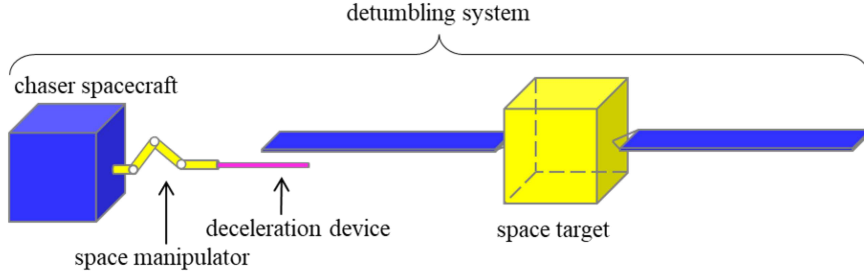


Fig. 1 Schematic diagram of the proposed detumbling method.

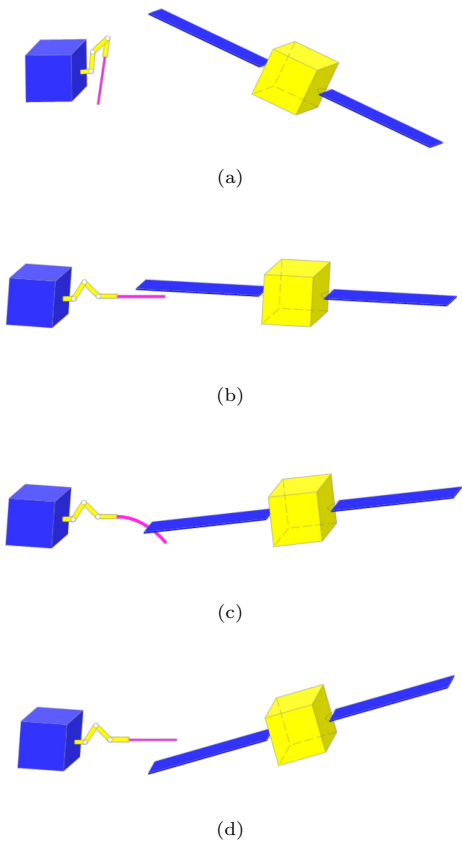


Fig. 2 Illustration of the detumbling process: preparation, pre-contact, contact, post-contact.

with \mathbf{I} being an 3×3 identity matrix. The global shape function $\mathbf{S}(x)$ has a complete set of rigid-body modes, and

$$\begin{cases} s_1 = 1 - 3\xi^2 + 2\xi^3 \\ s_2 = L(\xi - 2\xi^2 + \xi^3) \\ s_3 = 3\xi^2 - 2\xi^3 \\ s_4 = L(-\xi^2 + \xi^3) \end{cases} \quad (4)$$

where $\xi = x/L$ with $x \in [0, L]$, which is the coordinate of an arbitrary point on a element in the undeformed configuration.

The kinetic energy of a finite element can be expressed as

$$T_e = \frac{1}{2} \int_V \rho \dot{\mathbf{r}}^T \dot{\mathbf{r}} \, dx = \frac{1}{2} \dot{\mathbf{e}}^T \mathbf{M}_e \dot{\mathbf{e}} \quad (5)$$

then \mathbf{M}_e is the mass matrix of the element.

$$\mathbf{M}_e = \int_0^L \rho A \mathbf{S}^T \mathbf{S} \, dx \quad (6)$$

where ρ is the material density, and A is the cross-sectional area of the element.

In the model of the Euler-Bernoulli beam, the effect of the rotary inertia and the shear strain is neglected. Therefore, the beam cross-section is assumed to remain plane and perpendicular to the neutral axis.

Assuming isotropic materials, the bending strain energy of the beam element can be defined as

$$U_t = \frac{1}{2} \int_0^L EI_A \kappa^2 \, dx \quad (7)$$

where E is Young's modulus, I_A is the second moment of area, and κ is the curvature.

The transverse elastic force vector \mathbf{Q}_t is derived by differentiating U_t with respect to \mathbf{e} . Based on continuum mechanics, can be expressed as the product of the stiffness matrix and the element nodal coordinates vector [28],

$$\mathbf{Q}_t = \frac{\partial U_t}{\partial \mathbf{e}} = \mathbf{K}_t \mathbf{e} \quad (8)$$

Then, the stiffness matrix \mathbf{K}_t is written as

$$\mathbf{K}_t = EI_A \int_0^L \mathbf{S}_{xx}^T \mathbf{S}_{xx} \, dx \quad (9)$$

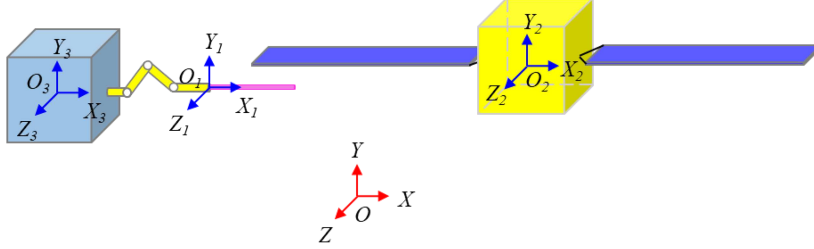


Fig. 3 Coordinate frames of the detumbling system.

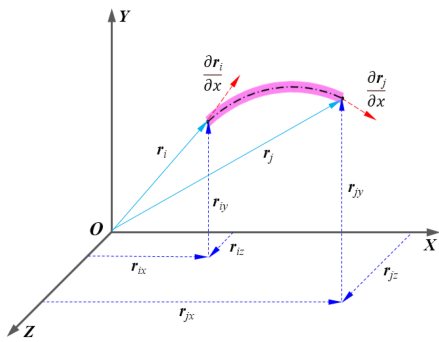


Fig. 4 Definition of element nodal coordinates.

The longitudinal strain energy of the beam element is defined as

$$U_l = \frac{1}{2} \int_0^L EA\varepsilon_l^2 dx \quad (10)$$

where ε_l is the longitudinal strain, which is defined using the Green-Lagrange strain tensor [28], as

$$\varepsilon_l = \frac{1}{2}(\mathbf{r}_x^T \mathbf{r}_x - 1) = \frac{1}{2}(\mathbf{e}^T \mathbf{S}_x^T \mathbf{S}_x \mathbf{e} - 1) \quad (11)$$

Then, the longitudinal elastic force vector \mathbf{Q}_l is derived by differentiating U_l with respect to \mathbf{e} ,

$$\mathbf{Q}_l = \frac{\partial U_l}{\partial \mathbf{e}} = \int_0^L EA\varepsilon_l \mathbf{S}_x^T \mathbf{S}_x \mathbf{e} dx = \mathbf{K}_l \mathbf{e} \quad (12)$$

Assuming that ε_l is constant throughout the beam element, and E and A are constants, it is possible to factor them out of the integral sign of Eq.(12). The stiffness matrix \mathbf{K}_l can be written as

$$\mathbf{K}_l = EA\bar{\varepsilon}_l \int_0^L \mathbf{S}_x^T \mathbf{S}_x dx \quad (13)$$

The average longitudinal strain along an element can be simply approximated as

$$\bar{\varepsilon}_l = \frac{l_s - L}{L} \quad (14)$$

l_s is the length of the deformed beam, which can be obtained by integrating the infinitesimal arc length ds along the neutral axis of the deformed element [29],

$$l_s = \int_l ds = \frac{1}{2} \int_0^L (\mathbf{e}^T \mathbf{S}_x^T \mathbf{S}_x \mathbf{e} + 1) dx \quad (15)$$

The external force vector \mathbf{Q}_e is defined using the virtual work as

$$\delta \mathbf{W}_e = \mathbf{F}_p^T \delta \mathbf{r}_p = \mathbf{F}_p^T \mathbf{S}_p \delta \mathbf{e} = \mathbf{Q}_e^T \delta \mathbf{e} \quad (16)$$

where \mathbf{F}_p is the external force acting on the point p ; \mathbf{r}_p is the position vector of the point p ; and \mathbf{S}_p is the shape function matrix of point p .

Using the expression of the kinetic energy, the strain energy, and the virtual work, the dynamical equation of a beam element can be obtained in matrix form as

$$\mathbf{M}_e \ddot{\mathbf{e}} + (\mathbf{K}_t + \mathbf{K}_l) \mathbf{e} = \mathbf{Q}_e \quad (17)$$

Based on the equation, the dynamical equation of the entire beam can be expressed as

$$\mathbf{M} \ddot{\mathbf{q}} + \mathbf{K} \mathbf{q} = \mathbf{Q} \quad (18)$$

where the \mathbf{q} is the vector of system coordinates, composed of all nodal coordinates of the beam. Similarly, the \mathbf{M} , \mathbf{K} and \mathbf{Q} are the mass matrix, the stiffness matrix and the external force vector of the entire beam, respectively.

Furthermore, the damping force can be considered to improve the dynamical model accurately. The Rayleigh damping model is introduced into the ANCF. In the linear finite element method, the Rayleigh damping matrix \mathbf{C} is defined for the structural damping as

$$\mathbf{C} = \alpha \mathbf{M} + \beta \mathbf{K} \quad (19)$$

where α and β are coefficients.

The dynamic equation of the beam with damping characteristics is written as

$$\mathbf{M}\ddot{\mathbf{q}} + \mathbf{C}\dot{\mathbf{q}} + \mathbf{K}\mathbf{q} = \mathbf{Q} \quad (20)$$

2.3 Dynamic model of detumbling system

As explained before, the thruster and the space manipulator adjustment process is not considered in this paper. So, the chaser satellite is simplified into a rigid robot with a flexible effector. The Lagrangian method is applied to model dynamic equations of the robot. Combined with Eq.(20), the dynamic model of the free-floating robot can be written as

$$\begin{cases} \mathbf{H}\ddot{\boldsymbol{\varphi}} = \mathbf{u} \\ \mathbf{M}\ddot{\mathbf{q}} + \mathbf{C}\dot{\mathbf{q}} + \mathbf{K}\mathbf{q} = \mathbf{Q} \\ \mathbf{q}_p - \mathbf{x}_p = 0 \\ \mathbf{q}_d - \boldsymbol{\tau}_p = 0 \end{cases} \quad (21)$$

where \mathbf{H} is the inertia matrix of the robot; $\boldsymbol{\varphi}$ is generalized coordinates vector of the robot; \mathbf{u} is the vector of control force and torques acting on the robot; $\mathbf{q}_p = [q_1, q_2, q_3]^T$ and $\mathbf{q}_d = [q_4, q_5, q_6]^T$ are position and direction vectors of the first nodal of the rod, respectively; \mathbf{x}_p and $\boldsymbol{\tau}_p$ are the position vector and the tangent vector of the end of the manipulator, respectively.

The dynamical model of the target is employed to compute the motion state of the target satellite in real time. It is assumed that the rigid satellite is free-floating in space. As depicted in Fig.3, the position and attitude model, described in the coordinate frame $O - XYZ$ and $O_2 - X_2Y_2Z_2$,

respectively, can be expressed as

$$\begin{cases} \mathbf{m}_t\ddot{\mathbf{r}}_t = \mathbf{F}_d \\ \dot{\boldsymbol{\theta}}_t = \mathbf{D}^2\boldsymbol{\omega}_t \\ {}^2\mathbf{J}_t {}^2\dot{\boldsymbol{\omega}}_t + {}^2\boldsymbol{\omega}_t^\times {}^2\mathbf{J}_t {}^2\boldsymbol{\omega}_t = {}^2\mathbf{T}_d \end{cases} \quad (22)$$

where \mathbf{m}_t and \mathbf{r}_t are the mass matrix and the centroid position vector of the target, respectively; \mathbf{F}_d is the vector of contact force on the target; $\boldsymbol{\theta}_t$ is the vector of Euler angles; \mathbf{D} is the coefficient matrix; ${}^2\mathbf{J}_t$ and ${}^2\boldsymbol{\omega}_t$ are the moment of inertia and the angular velocity of the target with respect to $O_2 - X_2Y_2Z_2$, respectively. ${}^2\boldsymbol{\omega}_t^\times$ is the anti-symmetric matrix of ${}^2\boldsymbol{\omega}_t$; ${}^2\mathbf{T}_d$ is the contact torque on the target with respect to $O_2 - X_2Y_2Z_2$.

3 Contact detection and modeling

In this section, the contact detection method, including coarse and fine detection is proposed to support contact force calculation and speed up the simulation. Furthermore, the contact force model is given as a necessary part of the detumbling dynamic model.

3.1 Contact detection method

The contact detection method checks whether the solar array's outer edge touches the rod and locates accurate contact points on the rod and the solar array edge. Before the contact occurs, the flexible rod is treated as a straight rod, but during the contact process, the rod becomes deformed.

During detumbling, the contact detection method is divided into two phases. The *coarse detection* phase is used first to detect the large overall motion to confirm whether the solar array edge is close to the rod. In the phase, large step size is used to speed up the numerical simulation.

As shown in Fig.5, $\overline{c1c2}$ represents the neutral axis of the straight rod. $\overline{e1e2}$ is the outer edge of the solar array near the deceleration device, and the point $e3$ is the middle point of $\overline{e1e2}$. $\overline{e3c3}$ is the distance from $e3$ to the rod, so $\overline{e3c3}$ is perpendicular to $\overline{c1c2}$ with the foot point $c3$ on the neutral axis. $\mathbf{r}_{c1}, \mathbf{r}_{c2}, \mathbf{r}_{c3}, \mathbf{r}_{e1}, \mathbf{r}_{e2}, \mathbf{r}_{e3}$ are defined as position vectors of $c1, c2, c3, e1, e2, e3$ in the global coordinate frame $O - XYZ$. $\mathbf{r}_{c1}, \mathbf{r}_{c2}, \mathbf{r}_{e1}$,

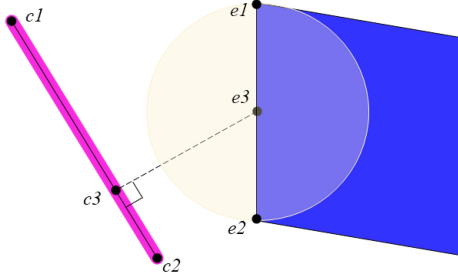


Fig. 5 Illustration of the coarse detection.

\mathbf{r}_{e2} , \mathbf{r}_{e3} are computed as follows

$$\begin{cases} \mathbf{r}_{c1} = \mathbf{r}_r + {}^I\mathbf{A}_3 {}^3\mathbf{p}_{c1} \\ \mathbf{r}_{c2} = \mathbf{r}_r + {}^I\mathbf{A}_3 {}^3\mathbf{p}_{c2} \\ \mathbf{r}_{e1} = \mathbf{r}_t + {}^I\mathbf{A}_2 {}^2\mathbf{p}_{e1} \\ \mathbf{r}_{e2} = \mathbf{r}_t + {}^I\mathbf{A}_2 {}^2\mathbf{p}_{e2} \\ \mathbf{r}_{e3} = (\mathbf{r}_{e1} + \mathbf{r}_{e2})/2 \end{cases} \quad (23)$$

where ${}^I\mathbf{A}_3$ and ${}^I\mathbf{A}_2$ are coordinate transformation matrices from $O_3 - X_3Y_3Z_3$ (fixed on the rod) and $O_2 - X_2Y_2Z_2$ (fixed on the target) to $O - XYZ$, respectively; \mathbf{r}_r and \mathbf{r}_t are positions of O_3 and O_2 in $O - XYZ$ respectively; ${}^3\mathbf{p}_{c1}$ and ${}^3\mathbf{p}_{c2}$ are vectors from O_3 to $c1$ and $c2$ in $O_3 - X_3Y_3Z_3$, respectively. ${}^2\mathbf{p}_{e1}$ and ${}^2\mathbf{p}_{e2}$ are vectors from O_2 to $e1$ and $e2$ in $O_2 - X_2Y_2Z_2$, respectively. The spheroid space was defined with the radius R_e :

$$R_e = \frac{\|\mathbf{r}_{e1} - \mathbf{r}_{e2}\|}{2} \quad (24)$$

When \mathbf{r}_{c1} , \mathbf{r}_{c2} , \mathbf{r}_{e1} , \mathbf{r}_{e2} and \mathbf{r}_{e3} satisfy the following condition, the rod has entered the neighborhood of the solar array edge, which means that the contact may occur.

$$\begin{cases} \frac{\|(\mathbf{r}_{c2} - \mathbf{r}_{c1}) \times (\mathbf{r}_{e3} - \mathbf{r}_{c1})\|}{\|\mathbf{r}_{c2} - \mathbf{r}_{c1}\|} < R_e \\ \frac{(\mathbf{r}_{c2} - \mathbf{r}_{c1})^T (\mathbf{r}_{e3} - \mathbf{r}_{c1})}{\|\mathbf{r}_{c2} - \mathbf{r}_{c1}\|} < \|\mathbf{r}_{c2} - \mathbf{r}_{c1}\| \end{cases} \quad (25)$$

After that, the *fine detection* phase will improve the detection accuracy and find contact points on the rod and the edge during the contact process. It should be noted that contact force will deform the flexible rod, so it cannot be treated as a straight rod in this phase.

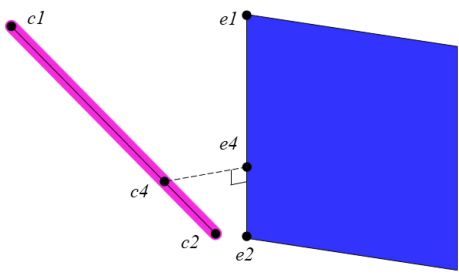


Fig. 6 Illustration of the fine detection.

As shown in Fig. 6, $c4$ is an arbitrary point on the neutral axis of the flexible rod, and $e4$ is the point on $\overline{e1e2}$ when $\overline{c4e4}$ is the distance from $c4$ to $\overline{e1e2}$. \mathbf{r}_{c4} and \mathbf{r}_{e4} are defined as the positions of $c4$ and $e4$ in the frame $O - XYZ$, respectively. According to the definition, points $c4$ and $e4$ can be determined by the following equation:

$$\begin{cases} \min f = \|\mathbf{r}_{c4} - \mathbf{r}_{e4}\| \\ \text{s.t. } \mathbf{r}_{c4} = \mathbf{S}(x)\mathbf{e}_j, \quad x \in [0, L] \\ (\mathbf{r}_{c4} - \mathbf{r}_{e4})^T (\mathbf{r}_{e2} - \mathbf{r}_{e1}) = 0 \\ (\mathbf{r}_{e4} - \mathbf{r}_{e1})^\times (\mathbf{r}_{e2} - \mathbf{r}_{e1}) = 0 \\ (\mathbf{r}_{e4} - \mathbf{r}_{e1})^T (\mathbf{r}_{e2} - \mathbf{r}_{e4}) > 0 \end{cases} \quad (26)$$

where \mathbf{e}_j is the j element nodal coordinates in ANCF, and $\mathbf{S}(x)$ is the shape function.

When the contact occurs, $c4$ and $e4$ become contact points on the rod and the edge, respectively. Then, the penetration depth that is applied to the calculation of contact force based on the Hertz theory can be obtained by Eq.(27):

$$\delta = \begin{cases} 0, & f \geq \Omega \\ \Omega - f, & f < \Omega \end{cases} \quad (27)$$

where Ω is determined by surface curvature radiiuses of the cylinder rod and the solar array edge. Finally, the contact process is finished when point $c4$ is very close to the endpoint $c2$ of the rod, as

$$\|\mathbf{r}_{c4} - \mathbf{r}_{c2}\| < \epsilon \quad (28)$$

where ϵ is a limited error.

3.2 Contact force model

The contact force model is applied to computing the contact force for the detumbling system. As

depicted in Fig. 7, the contact force \mathbf{F}_d acting on the target solar array edge $\overline{e1e2}$ at the contact point $e4$ (shown in Fig. 6) is the resultant force of the normal contact force \mathbf{F}_n and the friction force \mathbf{F}_t . \mathbf{F}_n are computed using the Hertz contact model and \mathbf{F}_t can be obtained by the Coulomb friction model.

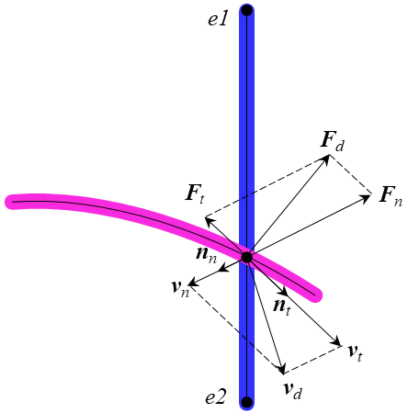


Fig. 7 Illustration of the contact force definition.

According to the contact detection method, the velocity of the outer solar array edge relative to the rod at the contact point is expressed as

$$\begin{cases} \mathbf{v}_d = \dot{\mathbf{r}}_{e4} - \dot{\mathbf{r}}_{c4} \\ \dot{\mathbf{r}}_{e4} = \dot{\mathbf{r}}_t + {}^2\omega_t^{\times} {}^2\mathbf{p}_{e4} \end{cases} \quad (29)$$

where $\dot{\mathbf{r}}_{e4}$ and $\dot{\mathbf{r}}_{c4}$ are velocities of contact points $e4$ and $c4$ (shown in Fig. 6), respectively. $\dot{\mathbf{r}}_t$ is the velocity of the centroid position O_2 of the target. ${}^2\mathbf{p}_{e4}$ is the vector from O_2 to $e4$ in the frame $O_2 - X_2Y_2Z_2$.

As shown in Fig. 6 and Fig. 7, \mathbf{v}_d consists of two components: the normal velocity \mathbf{v}_n in the direction of \mathbf{r}_{c4e4} , and the tangential velocity \mathbf{v}_t perpendicular to \mathbf{r}_{c4e4} . \mathbf{n}_n and \mathbf{n}_t are defined as the unit vectors in the direction of \mathbf{v}_n and \mathbf{v}_t , respectively. \mathbf{v}_n , \mathbf{v}_t , \mathbf{n}_n and \mathbf{n}_t are derived from Eq.(30).

$$\begin{cases} \mathbf{n}_n = \frac{\mathbf{r}_{c4} - \mathbf{r}_{e4}}{\|\mathbf{r}_{c4} - \mathbf{r}_{e4}\|} \\ \mathbf{v}_n = (\mathbf{v}_d \cdot \mathbf{n}_n)\mathbf{n}_n \\ \mathbf{v}_t = \mathbf{v}_d - \mathbf{v}_n \\ \mathbf{n}_t = \frac{\mathbf{v}_t}{\|\mathbf{v}_t\|} \end{cases} \quad (30)$$

As expressed before, the flexible rod contacts the solar array by turns. According to the Hertz theory, the normal contact force \mathbf{F}_n acting on the edge can be computed, as

$$\mathbf{F}_n = - \left(K_n \delta^{3/2} + C_n \frac{\delta^{3/2}}{\dot{\delta}_0} \dot{\delta} \right) \mathbf{n}_n \quad (31)$$

where $\dot{\delta}_0$ is the penetration velocity at the initial contact time; K_n and C_n are the equivalent stiffness and the damping coefficient,

$$\begin{cases} K_n = \frac{4}{3} \frac{E_1 E_2}{E_1 (1 - \nu_1^2) + E_2 (1 - \nu_2^2)} \sqrt{\frac{R_1 R_2}{R_1 + R_2}} \\ C_n = \frac{3}{4} K_n (1 - \sigma^2) \end{cases} \quad (32)$$

where E_1 and E_2 are Young's moduli of two bodies; ν_1 and ν_2 are Poisson's ratio; R_1 and R_2 are surface curvature radii; σ is the restitution coefficient.

According to the Coulomb friction model, the friction force \mathbf{F}_t acting on the edge can be given by

$$\mathbf{F}_t = -\mu \|\mathbf{F}_n\| \mathbf{n}_t \quad (33)$$

where μ is the friction coefficient.

The force acting on the contact point of the flexible rod is opposite to those acting on the solar array. In Eq.(22), \mathbf{F}_d is the resultant force of \mathbf{F}_n and \mathbf{F}_t . That is

$$\mathbf{F}_d = \mathbf{F}_n + \mathbf{F}_t \quad (34)$$

And the torque ${}^2\mathbf{T}_d$ on the target with respect to $O_2 - X_2Y_2Z_2$ can be written as

$${}^2\mathbf{T}_d = {}^2\mathbf{A}_I (\mathbf{r}_{e4} - \mathbf{r}_t) \times \mathbf{F}_d \quad (35)$$

where ${}^2\mathbf{A}_I$ is the coordinate transformation matrix from $O - XYZ$ to $O_2 - X_2Y_2Z_2$.

4 Numerical simulation and analysis

This section discusses the numerical simulation to validate the proposed detumbling method. Based on the simulation results, some characters of the method were analyzed.

4.1 Simulation conditions

The outer edge of a solar array contacts the middle of the flexible rod at every initial contact, and two solar arrays contact in return. The MATLAB was used to solve dynamical equations with the Runge-Kutta algorithm. Since the time step in the contact stage is much smaller than that in the contactless stage, time steps are set to $10^{-7}s$ and $10^{-4}s$, respectively. The rotating order $Z - Y - X$ is adopted to describe attitude angles $\theta_3 - \theta_2 - \theta_1$ from the global frame $O - XYZ$ to the frame $O_2 - X_2Y_2Z_2$ shown in the Fig.3. In addition, the physical parameters of the detumbling system are given in Table 1.

In the simulation, the controller is dedicated for the robot. During the contactless stage, the robot keeps tracking the centroid of the target, and the position and attitude remain stable in the contact stage. A six-dimension force/torque sensor is fitted between the end of the manipulator and the deceleration device to acquire force/torque data. Since the rod is sufficient light, it is ignored in the equation for the robot controller. According to Eq.(21), the dynamical model of the rigid robot can be described as

$$\mathbf{H}(\mathbf{x})\ddot{\mathbf{x}} = \mathbf{u} + \boldsymbol{\eta} \quad (36)$$

with $\mathbf{x} = [x, y, z, \theta_1, \theta_2, \theta_3]^T$ being the position coordinates and attitude angles, $\mathbf{u} = [u_1, u_2, u_3, u_4, u_5, u_6]^T$ being the inputs, and $\boldsymbol{\eta} = [\eta_1, \eta_2, \eta_3, \eta_4, \eta_5, \eta_6]^T$ being the force/torque acting on the centroid transformed from sensor data.

The *computed torque control* can be used to achieve tracking and stability control tasks. The law is written as

$$\mathbf{u} = \mathbf{H}(\mathbf{x})\mathbf{v} - \boldsymbol{\eta} \quad (37)$$

where

$$\mathbf{v} = \ddot{\mathbf{x}}_d - 2\lambda\dot{\tilde{\mathbf{x}}} - \lambda^2\tilde{\mathbf{x}} \quad (38)$$

where $\mathbf{v} = [v_1, v_2, v_3, v_4, v_5, v_6]^T$ is the equivalent input, $\tilde{\mathbf{x}} = \mathbf{x} - \mathbf{x}_d$ is the tracking error, and λ is a positive number. The error $\tilde{\mathbf{x}}$ then satisfies the equation

$$\ddot{\tilde{\mathbf{x}}} + 2\lambda\dot{\tilde{\mathbf{x}}} + \lambda^2\tilde{\mathbf{x}} = 0 \quad (39)$$

and thus converges to zero exponentially.

According to the detumbling process, the desired state \mathbf{x}_d is

$$\mathbf{x}_d = \begin{cases} \begin{bmatrix} r_{t1}(t) + d_1 \\ r_{t2}(t) + d_2 \\ r_{t3}(t) + d_3 \\ 0 \\ 0 \\ 0 \end{bmatrix}^T, & \text{in contactless phase} \\ \begin{bmatrix} r_{t1}(t_c) + d_1 \\ r_{t2}(t_c) + d_2 \\ r_{t3}(t_c) + d_3 \\ 0 \\ 0 \\ 0 \end{bmatrix}^T, & \text{in contact phase} \end{cases} \quad (40)$$

where $(r_{t1}(t), r_{t2}(t), r_{t3}(t))$ is the centroid position of the target; (d_1, d_2, d_3) is the vector of the trace point relative to the centroid position; t_c is the starting time of every fine detection phase.

4.2 Detumbling simulation and results

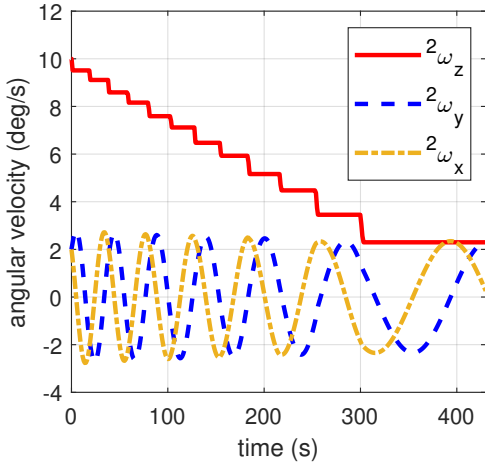
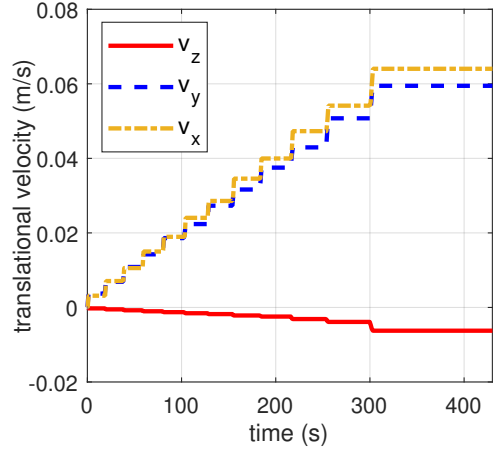
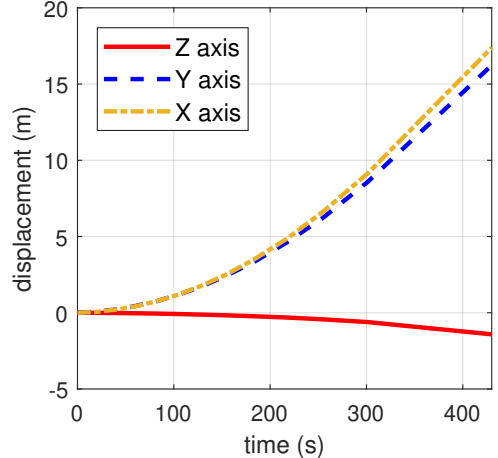
A tumbling satellite rotating with large nutation was not studied, because the solar array would move through a large spatial volume and would require a complex control strategy for the chaser spacecraft and the robot arm to adjust the position and direction of the deceleration device. That will be studied later in greater depth.

In simulation cases, the initial angular velocity of the target with respect to frame $O_2 - X_2Y_2Z_2$ is ${}^2\omega_t = [2, 2, 10]^T \text{deg/s}$. As shown in Fig.8, ${}^2\omega_z$, the angular velocity of the target in the Z_2 axis, decreases from 10deg/s to 2.2deg/s in about $300s$ with 12 contact processes, and amplitudes of ${}^2\omega_y$ and ${}^2\omega_x$ have no apparent changes from start to end. The result can verify that the detumbling method is valid and can efficiently decelerate the rotation. Moreover, the change of ${}^2\omega_z$ shows that the reduction in every contact process seems to increase with the decrease of ${}^2\omega_z$, which will be analyzed further in this section. Figure 9 shows that translational velocities increase with every contact process. V_x increases faster than V_y during the detumbling, which means the contact force F_x

Table 1 Physical parameters of the detumbling system

Component	Item (unit)	Parameter
Target satellite	Base : Length × width × thickness (m)	$1.5 \times 1.5 \times 1.5$
	Solar array: length × width × thickness (m)	$4.5 \times 2 \times 0.1$
	Mass (kg)	300
	Moment of inertia = $[J_{xx}, J_{yy}, J_{zz}]$ ($\text{kg} \cdot \text{m}^2$)	[300, 300, 600]
Robot	Solar array:Young's modulus E_1 (N/m^2)	7×10^{10}
	Base : Length × width × thickness (m)	$2 \times 2 \times 2$
	Manipulator linkage : Length × radius (m)	0.5×0.01
	Mass (kg)	1000
Flexible rod	Moment of inertia = $[J_{xx}, J_{yy}, J_{zz}]$ ($\text{kg} \cdot \text{m}^2$)	[1000, 1000, 1000]
	Length × radius (m)	1×0.01
	Density (kg/m^2)	500
	Young's modulus E_2 (N/m^2)	2×10^8

does more work than F_y . But the force in X direction cannot decelerate the rotation considering the set in Fig.3. As shown in Fig.10, displacements of the target centroid position change considerably, which means the robot must move over a wide range to complete the detumbling mission. As shown in Fig.11, the amplitude of θ_2 decreases and the amplitude of θ_1 increases over time, which indicates that the nutation of the target increases during detumbling. In particularly, θ_2 (Fig.11) indicates that the nutation increases rapidly after 310s when ${}^2\omega_z$ becomes similar in size to the amplitudes of ${}^2\omega_y$ and ${}^2\omega_x$ as shown in Fig.8. In addition, Fig.12 depicts the contact force acting on the target described in the frame $O - XYZ$. The force F_y may be large initially for every contact because of the impact.

**Fig. 8** Angular velocities of the target.**Fig. 9** Translational velocities of the target centroid position.**Fig. 10** Displacements of the target centroid position.

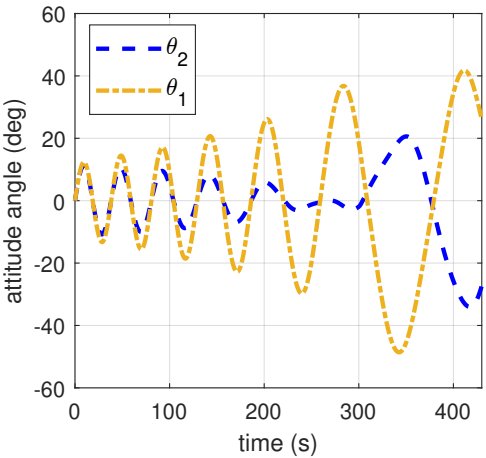


Fig. 11 Attitude angles of the target.

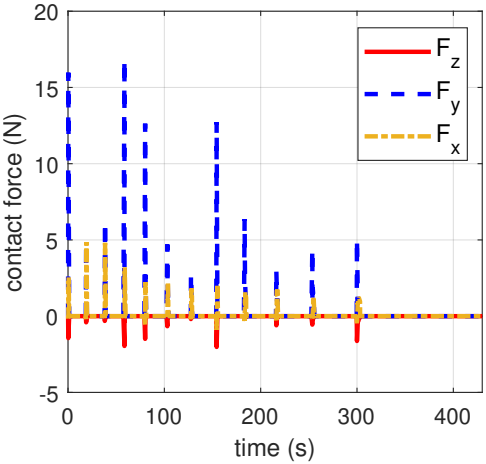


Fig. 12 Contact force on the target.

4.3 Contact process analysis

Based on our analysis, contact processes should be researched further to reveal features of the contact detumbling method proposed in this paper. Next, we simulate cases where the target rotates with an angular velocity only along to Z_2 axis to analyze dynamics.

Figure 13 shows decreasing ${}^2\omega_z$ with different initial angular velocities of the target without initial translational velocities in one contact stage. The decrease becomes large with the small initial rotating speed ${}^2\omega_z$, and the small initial ${}^2\omega_z$ causes that the contact stage lasts long as shown in the figure. That is because the impulse of the contact force will be larger with a longer contact time, which makes the angular momentum

decrease faster. However, if the contact accompanies translation of the target as shown in Fig.9, this law is not strict, as shown in Fig.8. It indicates that keeping the effector of the robot arm tracking the target in the contact stage may raise the detumbling efficiency.

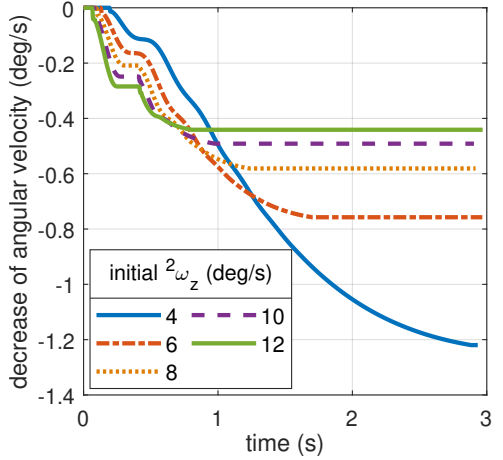


Fig. 13 Decreases of the ${}^2\omega_z$ with different initial ${}^2\omega_z$.

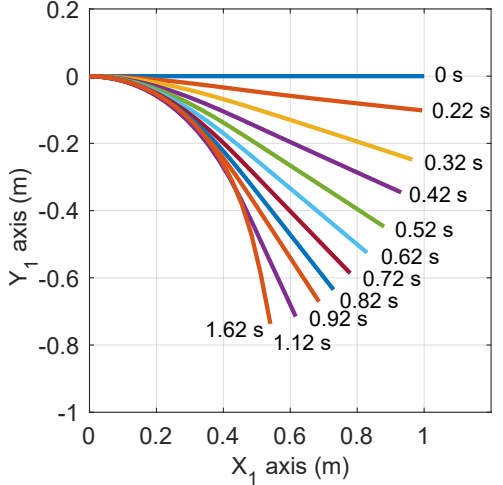


Fig. 14 Illustration of rod deformation in a contact process in the $O_1 - X_1 Y_1$ plane.

Figure 14 shows the deforming process of the rod in one contact stage, and Fig.15 presents contact forces F_y and F_x acting on the solar array edge and the deceleration torque 2T_z . The flexible deformation increasingly apparent, influencing the braking effect according to the detumbling system as presented in Fig.16. As shown in Fig.15,

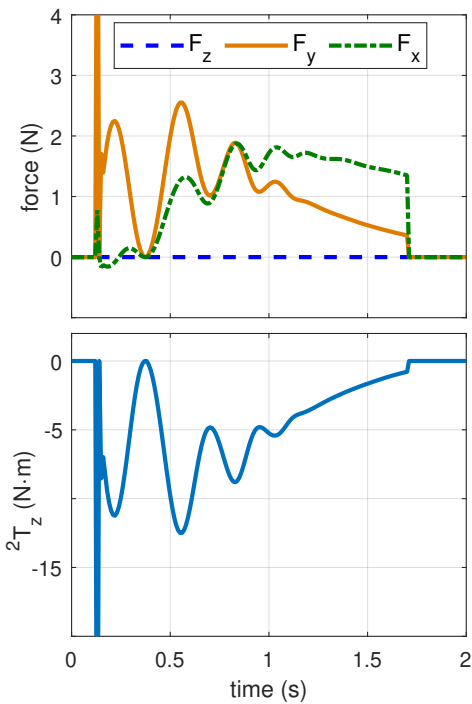


Fig. 15 Force and torque 2T_z on the target during a contact.

the force F_x increases with the deformation, but F_y decreases after $0.6s$, making the torque 2T_z decrease in the braking direction. This means that F_x does no work in the de-spinning mission. So, F_x can be used to enlarge the friction force to increase F_y .

The friction coefficient μ of Eq.(33) is set to different constants to simulate the contact process to verify this idea. As shown in Fig.17, a large μ makes the force F_x become small during the process, but that brings about the large F_y that increases the braking torque 2T_z validly. As a result, the angular velocity ${}^2\omega_z$ decreases more with a large μ as shown in Fig.18. Decreases are around $0.76deg/s$, $0.95deg/s$, $1.14deg/s$, and $1.32deg/s$ with friction coefficients 0.1 , 0.3 , 0.5 , and 0.7 , respectively.

5 Conclusion

This paper focuses on an accurate dynamic analysis of a method for detumbling non-cooperative malfunctioning satellites. As a new contact-type strategy, the flexible deceleration rod contacts the outer edge of the solar array to generate a large

braking torque. There are only five DOFs to be controlled, and a precise operation is carried out to avoid complicating the object's motion. The dynamic model is based on the ANCF and has successfully described precise large deformation and displacement of a rod with a low computational burden. The two-stage contact detection has provided accurate contact points as well as an efficient detumbling simulation. Numerical simulation has verified that the proposed detumbling method is validated and the detumbling efficiency is high enough. Moreover, analysis of the contact process has indicated that increasing the contact friction force could improve the detumbling effect, which should be considered further for flexible device design.

Acknowledgments. This work was supported by the National Natural Science Foundation of China [grant number 12072270 and U2013206]. We thank LetPub ([www.letpub.com](http://www letpub.com)) for its linguistic assistance during the preparation of this manuscript.

Conflict of interest. Authors declare that they have no conflict of interest.

Data availability. Data sharing is not applicable to this article as no datasets were generated or analyzed during the current study.

References

- [1] Houman H, M Reza E. Assessment of active methods for removal of LEO debris. *Acta Astronautica*. 2018;144:225–243. <https://doi.org/https://doi.org/10.1016/j.actaastro.2017.12.036>.
- [2] Acharya SP, Mukherjee A, Janaki MS. Accelerated magnetosonic lump wave solutions by orbiting charged space debris. *Nonlinear Dynamics*. 2021 Jul;105(1):671–689. <https://doi.org/10.1007/s11071-021-06594-x>.
- [3] Wang M, Luo J, Yuan J, Walter U. Detumbling strategy and coordination control of kinematically redundant space robot after capturing a tumbling target. *Nonlinear Dynamics*. 2018 May;92(3):1023–1043. <https://doi.org/10.1007/s11071-018-4106-4>.

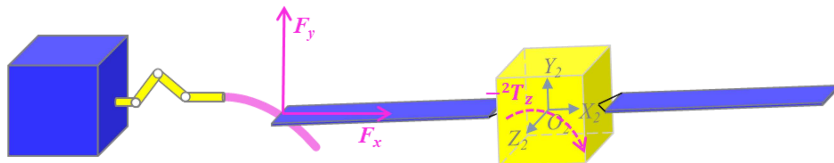


Fig. 16 Illustration of a contact case.

- [4] Forshaw JL, Aglietti GS, Fellowes S, Salmon T, Retat I, Hall A, et al. The active space debris removal mission RemoveDebris. Part 1: From concept to launch. *Acta Astronautica*. 2020;168:293–309. <https://doi.org/https://doi.org/10.1016/j.actaastro.2019.09.002>.
- [5] Lim J, Chung J. Dynamic analysis of a tethered satellite system for space debris capture. *Nonlinear Dynamics*. 2018 Dec;94(4):2391–2408. <https://doi.org/10.1007/s11071-018-4498-1>.
- [6] Flores-Abad A, Wei Z, Ma O, Pham K. Optimal Control of Space Robots for Capturing a Tumbling Object with Uncertainties. *Journal of Guidance, Control, and Dynamics*. 2014;37(6):2014–2017. <https://doi.org/10.2514/1.G000003>.
- [7] Flores-Abad A, Ma O, Pham K, Ulrich S. A Review of Space Robotics Technologies for On-Orbit Servicing. *Progress in Aerospace Sciences*. 2014 jul;68:1–26. <https://doi.org/10.1016/j.paerosci.2014.03.002>.
- [8] Li G, Xu P. Design and analysis of a deployable grasping mechanism for capturing non-cooperative space targets. *Aerospace Science and Technology*. 2020 Nov;106:106230. <https://doi.org/10.1016/j.ast.2020.106230>.
- [9] Ma C, Dai H, Wei C, Yuan J. Two-stage filter for inertia characteristics estimation of high-speed tumbling targets. *Aerospace Science and Technology*. 2019 Jun;89:333–344. <https://doi.org/10.1016/j.ast.2019.04.011>.
- [10] Ledkov A, Aslanov V. Evolution of space tethered system's orbit during space debris towing taking into account the atmosphere influence. *Nonlinear Dynamics*. 2019 May;96(3):2211–2223. <https://doi.org/10.1007/s11071-019-04918-6>.
- [11] Urrutxua H, Bombardelli C, Hedo JM. A preliminary design procedure for an ion-beam shepherd mission. *Aerospace Science and Technology*. 2019 May;88:421–435. <https://doi.org/10.1016/j.ast.2019.03.038>.
- [12] Liu X, Chang H, Huang P. Eddy current detumbling large geostationary debris based on feedback linearization model predictive control. *Aerospace Science and Technology*. 2021 May;112:106641. <https://doi.org/10.1016/j.ast.2021.106641>.
- [13] Chen G, Wang Y, Wang Y, Liang J, Zhang L, Pan G. Detumbling strategy based on friction control of dual-arm space robot for capturing tumbling target. *Chinese Journal of Aeronautics*. 2020 Mar;33(3):1093–1106. <https://doi.org/10.1016/j.cja.2019.04.019>.
- [14] Nishida SI, Kawamoto S. Strategy for Capturing of a Tumbling Space Debris. *Acta Astronautica*. 2011 jan;68(1):113–120. <https://doi.org/10.1016/j.actaastro.2010.06.045>.
- [15] Nakajima Y, Mitani S, Tani H, Murakami N, Yamamoto T, Yamanaka K. Detumbling Space Debris via Thruster Plume Impingement. In: AIAA/AAS Astrodynamics Specialist Conference. Long Beach, California: American Institute of Aeronautics and Astronautics; 2016. .

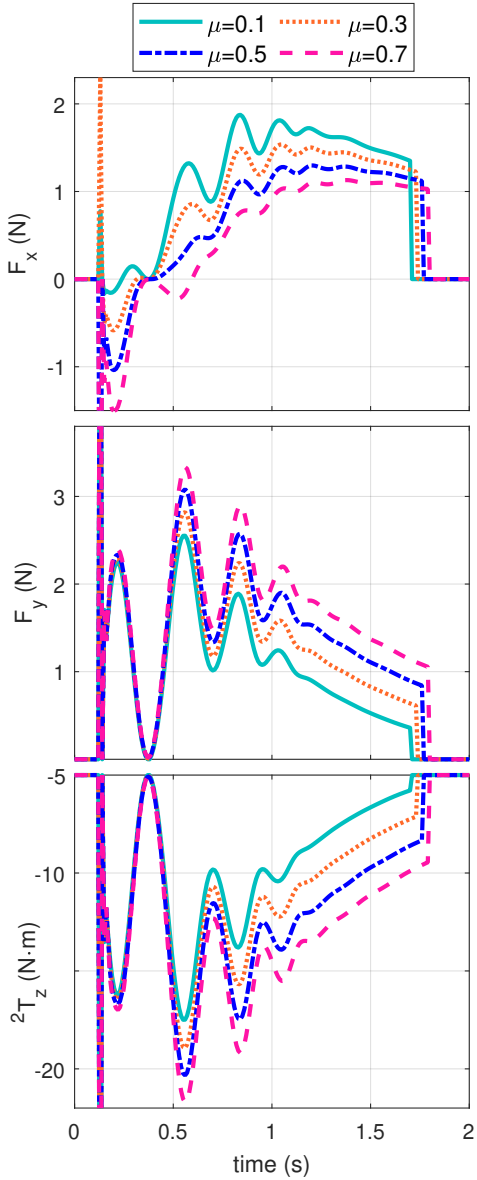


Fig. 17 Forces and torque 2T_z on the target during a contact process with different friction coefficients.

- [16] Nakajima Y, Tani H, Yamamoto T, Murakami N, Mitani S, Yamanaka K. Contactless Space Debris Detumbling: A Database Approach Based on Computational Fluid Dynamics. *Journal of Guidance, Control, and Dynamics*. 2018 Sep;41(9):1906–1918. <https://doi.org/10.2514/1.G003451>.

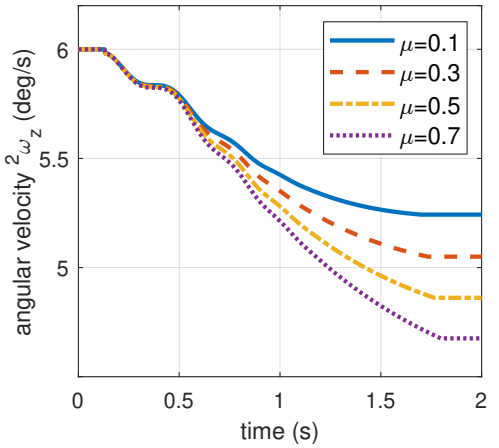


Fig. 18 Change of ${}^2\omega_z$ with different friction coefficients.

- [17] Bennett T, Schaub H. Touchless Electrostatic Three-dimensional Detumbling of Large Axisymmetric Debris. *The Journal of the Astronautical Sciences*. 2015 Sep;62(3):233–253. <https://doi.org/10.1007/s40295-015-0075-8>.
- [18] Gómez NO, Walker SJI. Earth's gravity gradient and eddy currents effects on the rotational dynamics of space debris objects: Envisat case study. *Advances in Space Research*. 2015 Aug;56(3):494–508. <https://doi.org/10.1016/j.asr.2014.12.031>.
- [19] Gómez NO, Walker SJI. Guidance, Navigation, and Control for the Eddy Brake Method. *Journal of Guidance, Control, and Dynamics*. 2016 Sep;40(1):52–68. <https://doi.org/10.2514/1.G002081>.
- [20] Gómez NO, Walker SJI. Eddy currents applied to de-tumbling of space debris: Analysis and validation of approximate proposed methods. *Acta Astronautica*. 2015 Sep;114:34–53. <https://doi.org/10.1016/j.actaastro.2015.04.012>.
- [21] Kumar R, Sedwick RJ. Despinning Orbital Debris Before Docking Using Laser Ablation. *Journal of Spacecraft and Rockets*. 2015;52(4):1129–1134. <https://doi.org/10.2514/1.A33183>.
- [22] Kirk H, Steve U. Attitude Stabilization of an Uncooperative Spacecraft in an Orbital Environment using Visco-Elastic Tethers. In:

- AIAA Guidance, Navigation, and Control Conference. San Diego, California, USA; 2016. .
- [23] Wang D, Huang P, Meng Z. Coordinated stabilization of tumbling targets using tethered space manipulators. *IEEE Transactions on Aerospace and Electronic Systems*. 2015;51(3):2420–2432. <https://doi.org/10.1109/TAES.2015.140530>.
- [24] Wu H, Sun S, Wei C, Zhang H, Zhao Y. Tumbling target despun based on robotic flexible brush. *Acta Aeronautica et Astronautica Sinica* (in Chinese). 2019;40(5):422587. <https://doi.org/10.7527/S1000-98-6893.2018.22587>.
- [25] Liu Y, Yu Z, Liu X, Cai G. Active Detumbling Technology for High Dynamic Non-Cooperative Space Targets. *Multibody System Dynamics*. 2019 Sep;47(1):21–41. <https://doi.org/10.1007/s11044-019-09675-3>.
- [26] Liu Y, Yu Z, Liu X, Chen J, Cai G. Active Detumbling Technology for Noncooperative Space Target with Energy Dissipation. *Advances in Space Research*. 2019 Mar;63(5):1813–1823. <https://doi.org/10.1016/j.asr.2018.11.017>.
- [27] Wang X, Zhou Z, Chen Y, Chen S. Optimal Contact Control for Space Debris Detumbling and Nutation Damping. *Advances in Space Research*. 2020 Aug;66(4):951–962. <https://doi.org/10.1016/j.asr.2020.04.043>.
- [28] Berzeri M, Shabana AA. DEVELOPMENT OF SIMPLE MODELS FOR THE ELASTIC FORCES IN THE ABSOLUTE NODAL COORDINATE FORMULATION. *Journal of Sound and Vibration*. 2000 Aug;235(4):539–565. <https://doi.org/10.1006/jsvi.1999.2935>.
- [29] Wago T, Kobayashi N, Sugawara Y. Improvement on Evaluating Axial Elastic Force in Bernoulli-Euler Beam Based on the Absolute Nodal Coordinate Formulation by Accurate Mean Axial Strain Measure. In: Volume 4: 8th International Conference on Multibody Systems, Nonlinear Dynamics, and Control, Parts A and B. Washington, DC, USA: ASMEDC; 2011. p. 963–970.
- [30] Sopanen JT, Mikkola AM. Description of Elastic Forces in Absolute Nodal Coordinate Formulation. *Nonlinear Dynamics*. 2003 Oct;34(1):53–74. <https://doi.org/10.1023/B:NODY.0000014552.68786.bc>.